

The analogy between the ‘hidden order’ and the orbital antiferromagnetism in URu₂Si₂

H.-H. Kung,^{1,*} S. Ran,^{2,3} N. Kanchanavatee,^{2,3} V. Krapivin,¹ A. Lee,¹

J. A. Mydosh,⁴ K. Haule,¹ M. B. Maple,² and G. Blumberg^{1,5,†}

¹*Department of Physics & Astronomy,*

Rutgers University, Piscataway, NJ 08854, USA

²*Department of Physics, University of California San Diego, La Jolla, CA 92093, USA*

³*Center for Advanced Nanoscience, University of California San Diego, La Jolla, CA 92093, USA*

⁴*Kamerlingh Onnes Laboratory, Leiden University, 2300 RA Leiden, The Netherlands*

⁵*National Institute of Chemical Physics and Biophysics, 12618 Tallinn, Estonia*

In URu₂Si₂ two types of staggered phases involving long range ordering of the uranium-5f electrons compete at low temperature when a critical parameter x is tuned, where x can be chemical substituent concentration¹, pressure² or magnetic field³. When cooled at below the critical value x_c , the non-magnetic ‘hidden order’ (HO) phase with broken local chiral symmetry emerges⁴, whereas above x_c , unconventional antiferromagnetic (AF) phase with broken local time-reversal symmetry appears⁵. The two phases show strikingly similar electronic properties⁶. ‘Janus faces’ nature of the HO and AF phases has been theorized before^{7,8}, but the experimental signatures of the interplay between them are still lacking. Here, we use polarized Raman scattering to study the dynamical fluctuations between the two competing ground states as a function of x . Albeit the distinct discrete symmetries are broken above and below x_c , we detect a resonance continuously evolving with parameter x , providing evidence for a unified order parameter across the URu₂Si₂ phase diagram.

URu₂Si₂ holds long-standing interest in the strongly correlated electron community due to several emergent types of long range order it exhibits. Below the second order phase transition temperature $T_{DW}(x)$, two density-wave-like orders emerge⁹: the enigmatic ‘hidden order’ (HO) phase below about 17.5 K¹⁰⁻¹², and the onset of an unconventional large moment antiferromagnetic (LMAF) phase with the application of hydrostatic pressure⁵ or uniaxial

stress¹³. Below 1.5 K, a superconducting state, which likely breaks time reversal symmetry¹⁴, emerges from the HO phase. Recently, much effort has been dedicated towards unraveling the order parameter of the HO phase through several newly developed experimental and theoretical techniques^{14–19}. In particular, the symmetry analysis of the low temperature Raman scattering data implies that the reflection symmetries of tetragonal D_{4h} point group (No. 139 I4/mmm) associated with the paramagnetic (PM) state are broken, and a chirality density wave emerges as the HO ground state⁴.

The HO and LMAF phases are known to exhibit ‘adiabatic continuity’⁶, i.e., both phases possess similar electronic properties^{1,20}, and Fermi surfaces practically show no change across the phase boundary⁶. Furthermore, inelastic neutron scattering observed a dispersive exciton in the HO phase^{13,21} and recently in the LMAF phase of pressurized URu₂Si₂²². This raises the intriguing question of the symmetry relation between the two phases. However, experimental progress is hindered due to inherent constraints of low temperature pressurized experiments.

The availability of URu_{2–x}Fe_xSi₂ crystals^{1,23} made it possible to perform high-resolution spectroscopic experiments at low temperature and ambient pressure in both the HO and LMAF phases. Iron substitution mimics the effect of applying small pressure or in-plane stress on the URu₂Si₂ lattice, and the iron concentration, x , can be approximately treated as an effective ‘chemical pressure’¹. Recently, the phase diagram of URu_{2–x}Fe_xSi₂ single crystals have been determined^{9,23–26}, which resembles the low pressure phase diagram of pristine URu₂Si₂^{5,19} (Fig. 1a). The inelastic neutron scattering measurements again illustrate the analogies of the LMAF phase to the HO phase^{26,27}, albeit differences remain relating to the existence of the resonance in the LMAF state of pressurized^{22,27} or Fe-substituted crystals²⁶.

Figure 1h shows the temperature dependence of the Raman response in the eminent A_{2g} symmetry channel of the D_{4h} group, which transforms as a pseudo-vector, i.e., odd under all vertical and diagonal reflections of the square lattice²⁹. The upper panels show the intensity plots of the low energy Raman response, $\chi''_{A_{2g}}(\omega, T)$, below 30 K. Above $T_{DW}(x)$, a quasi-elastic peak (QEP) comprises most of the spectral weight for all samples, narrowing towards the transition. The observed QEP originates from overdamped excitations between quasi-degenerate crystal field states^{4,7}, and the narrowing of the QEP with cooling is due to the increase of excitation lifetime, related to the development of a hybridization gap and formation of a heavy Fermi liquid^{30,31}.

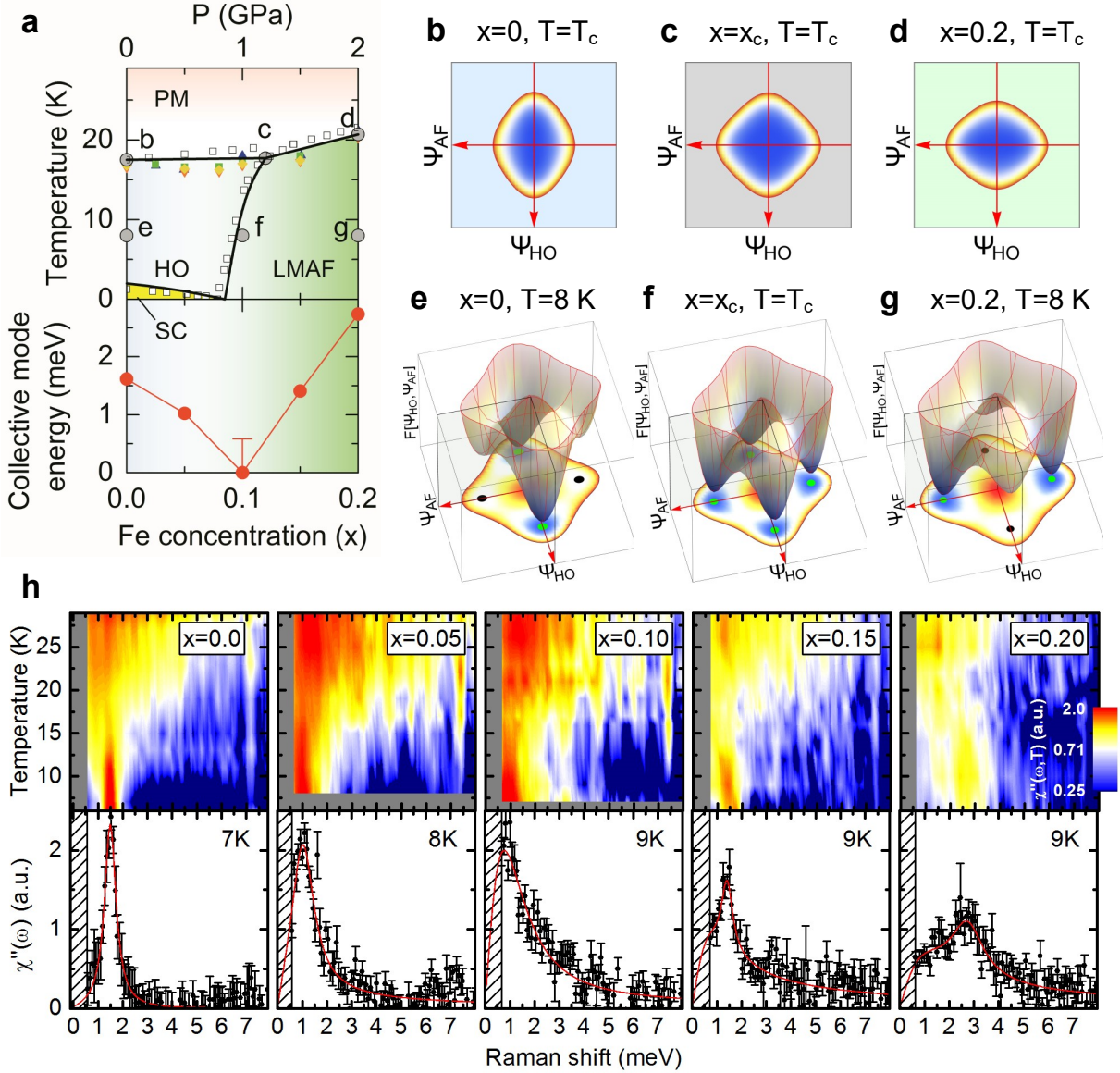


FIG. 1. The phase diagram of $\text{URu}_{2-x}\text{Fe}_x\text{Si}_2$ and temperature dependence of the A_{2g} Raman susceptibility. **a**, The upper panels show the phase diagram of URu_2Si_2 system, where the black lines show the phase boundaries. The measurements on the iron substituted $\text{URu}_{2-x}\text{Fe}_x\text{Si}_2$ crystals from neutron diffraction²⁵ (blue triangle), electrical resistivity¹ (green square), magnetic susceptibility¹ (purple triangle) and heat capacity²³ (yellow diamond), are overlaid with the neutron diffraction results for URu_2Si_2 under hydrostatic pressure⁵ (open square) to show the similarity between the two tuning parameters. The lower panel shows the dependence of the A_{2g} collective mode energy on the iron concentration, x . At the critical concentration, $x = 0.1$, the mode maximum is below the accessible energy cutoff. Therefore, the data point is placed at zero energy, with the error bar reflecting the instrumental cutoff.

FIG. 1. (Previous page.) **b-g**, Schematics of the Ginzburg-Landau free energy (Eq. 1) at various special points in the phase diagram (solid gray circles in **a**). ψ_{HO} and ψ_{AF} are the real and imaginary part of the hexadecapole order parameter, respectively^{7,28}. **h**, The low temperature Raman response in the A_{2g} symmetry channel, $\chi''_{A_{2g}}(\omega, T)$. The upper panels show intensity plots, where the intensities are color coded in logarithmic scale. The lower panels show the spectra at about half the transition temperature to emphasize the collective mode, where the error bars represent one standard deviation. The red solid lines are guides to the eye.

Below $T_{DW}(x)$, the most significant feature in the A_{2g} channel is a sharp collective-mode. The sharpness of this resonance suggests the lack of relaxation channels due to the opening of an energy gap^{9,30,32}. In order to see the mode's line-shape more clearly, we plot $\chi''_{A_{2g}}(\omega, T)$ for each iron concentration x in the lower panels, with $T \approx T_{DW}(x)/2$. The line-shapes broaden with increasing x owing to the inhomogeneity of the local stress field, or unsuppressed relaxation channels introduced by doping that interact with the collective mode, which may also be related to the increasing continuum in the $x = 0.15$ and 0.2 spectra. In contrast to the monotonic broadening of the line-shape width, the collective mode frequency shows non-monotonic behavior as function of x . The lower panel of Fig. 1a plots the mode energy against iron concentration. The energy decreases with increasing x in the HO phase, till vanishes below the instrumental resolution at iron concentration $x = 0.10$, which is close to the HO and LMAF phase boundary determined by elastic neutron scattering²⁵ and thermal expansion measurements²³. The resonance reappears in the LMAF phase, where the energy increases with increasing x . The resonance in the LMAF state appears in the same A_{2g} symmetry channel as the collective mode in the HO phase.

The similarity of the Raman response in the HO and LMAF phases encourages us to compare our results with the magnetic susceptibility. Figure 2 shows the temperature dependence of the real part of the static A_{2g} Raman susceptibility $\chi'_{A_{2g}}(0, T)$, compared with the c -axis magnetic susceptibility $\chi_c^m(T)$ ²³. While there are discrepancies around the maxima at about 50–100 K, both quantities follow the same Curie-Weiss-like temperature dependence above 100 K, followed by a suppression approaching the second order phase transition.

The comparison between $\chi'_{A_{2g}}(0, T)$ and $\chi_c^m(T)$ has been studied within the frame work of a phenomenological minimal model^{4,7}. This is composed of two low-lying singlet or-

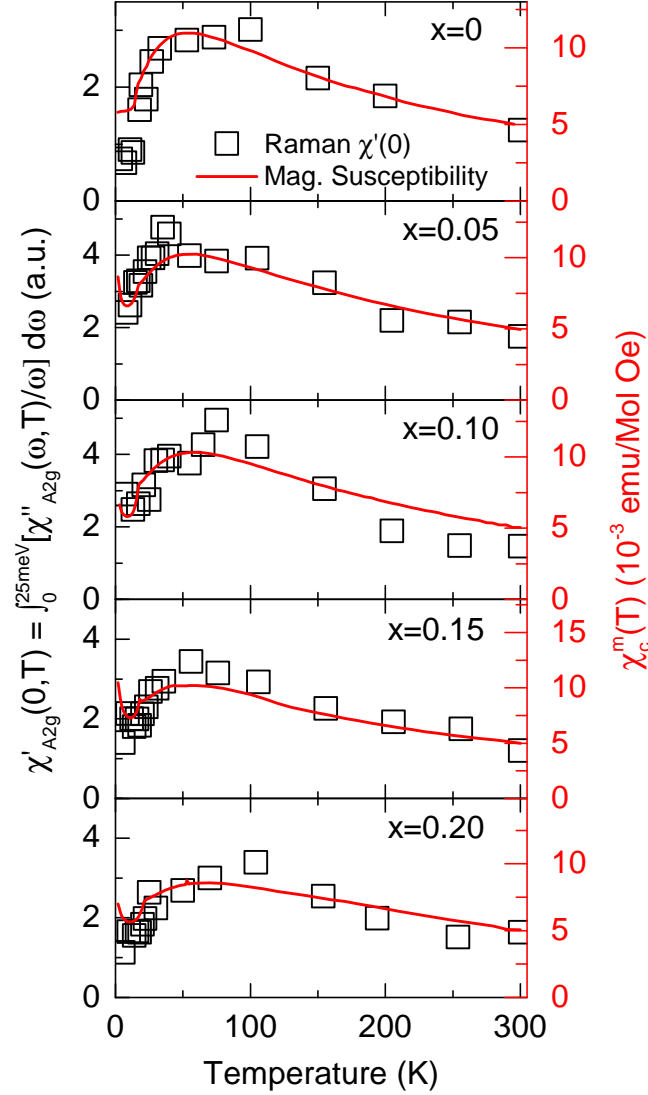


FIG. 2. **Temperature dependence of the static A_{2g} Raman susceptibility.** The static Raman susceptibility in the A_{2g} symmetry channel (open squares), $\chi'_{A_{2g}}(0, T) = \int_0^{25 \text{ meV}} \frac{\chi''_{A_{2g}}(\omega, T)}{\omega} d\omega$, compared with the magnetic susceptibility with field applied along the c -axis²³ (solid line). Note the unconventional temperature dependence of the susceptibilities due to the formations of the heavy fermion states below about 50 K³³.

bit levels on uranium sites, separated by an energy scale of $\omega_0 = 35 \text{ K}$. These states with pseudo-vector-like A_{2g} and full-symmetric A_{1g} symmetries are denoted by $|A_{2g}\rangle$ and $|A_{1g}\rangle$, respectively. At high temperatures, the crystal field states are quasi-degenerate in energy and localized at the uranium f -shells in space. The Curie-Weiss-like behavior above 100 K in static magnetic²³ and Raman-susceptibilities^{4,34,35} suggest A_{2g} pseudo-vector-like

instabilities at low temperature. Below about 50 K, the Kondo screening begins setting in^{19,30,32,36} and the correlation length of the HO³⁷ or LMAF^{5,38} phase builds at ordering vector $Q_0 = (0, 0, 1)$, and therefore both the magnetic and Raman uniform susceptibilities start to decrease (Fig. 2). Close to the transition temperature, both the HO and LMAF order parameters fluctuates regardless of the low temperature ordering (Fig. 1b-d). However, the static magnetic susceptibility at Q_0 only diverges across the PM–LMAF phase transition^{5,25}, whereas it becomes ‘near critical’ from PM–HO phase³⁷. Thus, HO is a non-magnetic transition, but there is the ‘ghost’ of LMAF present as shown in Fig. 1b. Here, we find that the temperature dependencies of the static A_{2g} Raman susceptibility $\chi'_{A_{2g}}(0, T)$ are similar and track $\chi_c^m(T)$ in all measured samples, suggesting that the minimal model is applicable for the studied iron substituted crystals.

We now discuss the origin and the observed doping dependence of the collective mode in the ordered phases within a phenomenological Ginzburg-Landau approach. Within the minimal model, the two order parameters can be constructed from $|A_{2g}\rangle$ and $|A_{1g}\rangle$ ⁷. The HO phase was explained as the state in which the two levels mix, resulting in a lower symmetry point group on uranium site, which breaks all vertical and diagonal reflection symmetry planes, and thus acquires left- and right-handedness.^{4,7} The staggering of left and right handedness solutions on the lattice gives rise to the chirality density wave⁴ (see Fig. 3a). In the HO phase, the staggered condensate can be approximated by a form $|\psi_{HO}\rangle = \prod_{r=A \text{ site}} |\text{HO}_r^+\rangle \times \prod_{r=B \text{ site}} |\text{HO}_r^-\rangle$. Note that $|\text{HO}_r^\pm\rangle$ at uranium site r is dominantly $|A_{2g}\rangle$, with small admixture of $|A_{1g}\rangle$, i.e., $|\text{HO}^\pm\rangle = \cos\theta |A_{2g}\rangle \pm \sin\theta |A_{1g}\rangle$.

In the HO the orbital mixing is purely real. If, however the mixing is purely imaginary, the charge distribution on the uranium site does not break any spatial symmetry, instead; it acquires non-zero out-of-plane magnetic moments, and thereby breaks time reversal symmetry. The Néel-type condensate (see Fig. 3b) takes the form $|\psi_{AF}\rangle = \prod_{r=A \text{ site}} |\text{AF}_r^+\rangle \times \prod_{r=B \text{ site}} |\text{AF}_r^-\rangle$, where $|\text{AF}^\pm\rangle = \cos\theta |A_{1g}\rangle \pm i \sin\theta |A_{2g}\rangle$ ⁷. The two apparently competing orders, the chirality density wave and the antiferromagnetic state, are both constructed by mixing the two orbital states on uranium sites with a real or an imaginary phase, thus unifying the two order parameters.

The Ginzburg-Landau free energy can then be constructed from the two component order parameter $\Psi^T \equiv \begin{pmatrix} \psi_{HO} & \psi_{AF} \end{pmatrix}$, where the order parameters correspond to the two

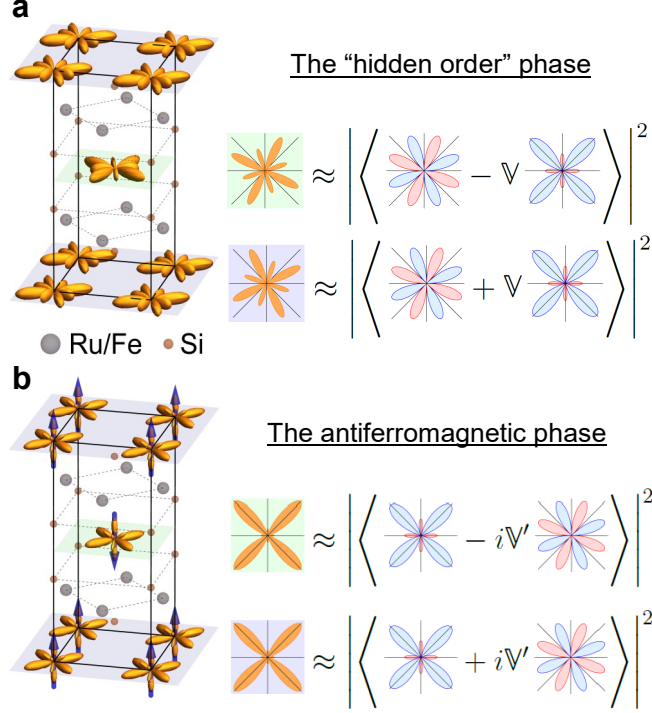


FIG. 3. **Crystal structure and ground states of the HO and LMAF phases.** The crystal structure of $\text{URu}_{2-x}\text{Fe}_x\text{Si}_2$ in **a**, the HO and **b**, the LMAF phases. Illustrations capturing the symmetries of the charge distributions of the ground state wave functions are placed at the uranium atomic sites. On the right of the crystal lattices are illustrations showing the in-plane structures of the wave functions. In the HO phase, the crystal field state with the lowest energy has A_{2g} symmetry with 8 nodal lines, $|A_{2g}\rangle$, which mixes with the first excited state with A_{1g} symmetry, $|A_{1g}\rangle$, to form the local wave functions in the HO phase, $|\text{HO}^\pm\rangle \approx \cos\theta |A_{2g}\rangle \pm \sin\theta |A_{1g}\rangle$. In the LMAF phase, the ordering of the crystal field states switches, and the new wave functions in the LMAF phase are, $|\text{AF}^\pm\rangle \approx \cos\theta |A_{1g}\rangle \pm i\sin\theta |A_{2g}\rangle$. Here, $\theta \equiv \arcsin(V/\omega_0)$ and $\theta' \equiv \arcsin(V'/\omega_0)$, respectively. ω_0 is the splitting between the lowest lying crystal field states in the minimal model. V and V' are the order parameter strength in the HO and LMAF phases, respectively. $|A_{2g}\rangle$ and $|A_{1g}\rangle$ are the A_{2g} and A_{1g} symmetrized crystal field states in the minimal model, respectively. In the figure, we let $\sin\theta \approx V$ and $\sin\theta' \approx V'$ to simplify the representation.

condensates $|\psi_{HO}\rangle$ and $|\psi_{AF}\rangle$ defined above. The free energy takes the form

$$F[\Psi] = \Psi^T \hat{A} \Psi + \beta (\Psi^T \Psi)^2 + \gamma (\Psi^T \hat{\sigma}_1 \Psi)^2 \quad (1)$$

where $\hat{A} \equiv \begin{pmatrix} \alpha_{HO} & 0 \\ 0 & \alpha_{AF} \end{pmatrix}$, with α_{HO} and α_{AF} vanish at the critical temperature. $\hat{\sigma}_1 \equiv \begin{pmatrix} 0 & 1 \\ 1 & 0 \end{pmatrix}$ is the Pauli matrix. γ controls a finite barrier between the two minima in Fig.1e-g, hence ensures phase separation between the HO and LMAF phases³⁸. The free energy parameters are introduced following the recipes given in Haule and Kotliar^{28,39} with adjustments to match the phase diagram in Fig. 1a (Materials and Methods).

Figure 1b-g plots the Ginzburg-Landau free energy in two dimensional space of ψ_{HO} and ψ_{AF} . Below the second-order phase transition, two global and two local minima develop on ψ_{HO} and ψ_{AF} axes due to spontaneous discrete symmetry breaking, where the minima characterize the ground states in the HO and LMAF phases, respectively.

At the critical doping (Fig. 1f), the four minima are degenerate, but the barrier between the minima remains finite due to a γ term in Ginzburg-Landau functional. Therefore the transition between HO and LMAF phases is of the first order, and the coexistence of both phases is allowed, explaining the LMAF puddles that have been observed in the HO phase^{40,41}.

The energy separation between the dominant long range order (e.g., $|\psi_{HO}\rangle$) and the subdominant order (e.g., $|\psi_{AF}\rangle$) is vanishingly small at the critical Fe concentration, and even away from this point can be smaller than the size of the gap. The exciton of subdominant symmetry (e.g., $|\psi_{AF}\rangle$) can form in the gap, which then propagates through the order of the dominant symmetry (e.g., $|\psi_{HO}\rangle$). Likewise, when the ground state is of $|\psi_{AF}\rangle$, the propagating exciton is of $|\psi_{HO}\rangle$ symmetry. The symmetry difference between the two condensates is A_{2g} -like, hence such exciton can be detected by Raman in the A_{2g} channel, and explains the sharp resonance shown in Fig.1 h. It is clear from this discussion that the energy of the resonance vanishes at the critical iron concentration, and is linearly increasing away from the critical point. For superconductors, such an excitation is known as the Bardasis-Schrieffer mode, characterizing the transition between two competing Cooper pairing channels⁴².

More generally, the uranium 5f orbitals in solids can arrange in surprising types of orders, including orders with broken chirality or time reversal symmetry. While such orders are competing for the same phase space in URu₂Si₂, they are also subtly connected and were here unified into a common order parameter, which can be switched with small energy cost. The low energy excitations are usually Goldstone modes, but here we detected a new type of

excitation, which connects two types of long range order, and is observed as a resonance by light scattering. The resonance brings light to a long-standing problem of emergent phases of exotic local orbital self-organization and their interrelation.

Acknowledgments

We are grateful for discussions with C. Broholm, N.P. Butch, P. Coleman, I.R. Fisher, P.B. Wiegmann and V.M. Yakovenko. G.B. and H.-H.K. acknowledge support from DOE BES Award DE-SC0005463. A.L. and V.K. acknowledge NSF Award DMR-1104884. K.H. acknowledges NSF Award DMR-1405303. M.B.M., S.R. and N.K. acknowledge DOE BES Award DE-FG02-04ER46105 (crystal growth) and NSF Award DMR-1206553 (materials characterization).

Author Contributions

G.B. and M.B.M. designed and supervised the experiments. K.H., G.B. and H.-H.K. developed the G.-L. theory. H.-H.K., V.K. and A.L. acquired and analyzed the Raman scattering data. S.R., N.K. and M.B.M. prepared the single crystals and acquired the magnetic susceptibility data. All authors contributed to the discussion and writing of the manuscript.

Competing financial interests

The authors declare no competing financial interests.

Methods

Single crystals of Fe substituted URu_2Si_2 were grown in a tetra-arc furnace using the Czochralski method in an argon atmosphere. The quality of the synthesized single crystals was confirmed by x-ray diffraction measurements in a Bruker D8 Discover diffractometer.

The Raman spectra were acquired in a quasi-backscattering geometry along the crystallographic c -axis, using a continuous flow liquid helium optical cryostat. For excitation, the 752.5 nm (about 1.65 eV) Kr^+ ion laser line was used, with the spot size roughly $50 \times 100 \mu\text{m}^2$. The power on the samples is about 12 mW for most temperatures, and kept below 6 mW to achieve the lowest temperatures. All temperatures shown were corrected for laser heating. The scattered light was analyzed and collected by a custom triple-grating spectrometer equipped with a liquid nitrogen cooled CCD detector. The intensities were corrected for the spectral response of the spectrometer and CCD.

We adopt Porto's notation to indicate the scattering geometries, where the directional vectors of incident and scattered light polarizations are denoted by \mathbf{e}_i and \mathbf{e}_s , respectively. $X=[100]$ and $Y=[010]$ are aligned along crystallographic a -axis, $X'=[110]$ and $Y'=[1\bar{1}0]$ are aligned 45° to the a -axis, $R=(X+iY)/\sqrt{2}$ and $L=(X-iY)/\sqrt{2}$ are right and left circularly polarized, respectively. The measured spectral intensity in the $\mathbf{e}_i\mathbf{e}_s$ scattering geometry, $I_{\mathbf{e}_i\mathbf{e}_s}(\omega, T)$, is related to the Raman response function, $\chi''_{\mathbf{e}_i\mathbf{e}_s}(\omega, T) \equiv \text{Im}[\chi_{\mathbf{e}_i\mathbf{e}_s}(\omega, T)]$, by the following: $I_{\mathbf{e}_i\mathbf{e}_s}(\omega, T) = [1 + n(\omega, T)]\chi''_{\mathbf{e}_i\mathbf{e}_s}(\omega, T) + L(\omega, T)$, where $\chi_{\mathbf{e}_i\mathbf{e}_s}(\omega, T)$ is the Raman susceptibility, $n(\omega, T)$ is the Bose factor, and $L(\omega, T)$ is a background mainly resulting from luminescence of the sample. In the D_{4h} group, the Raman response in different scattering geometries are composed of the excitations from distinct symmetry channels as dictated by the Raman tensors⁴³. The excitations accessible to Raman scattering from the ab -plane can be decomposed into 4 irreducible representations, i.e., A_{1g} , A_{2g} , B_{1g} and B_{2g} . However, we noticed that other than the phononic contribution, the response in B_{1g} and B_{2g} symmetry channels are the same and weakly temperature dependent. This suggests that electronic Raman contributions in the B_{1g} and B_{2g} channels are negligibly small, and the measured spectral intensity in RL scattering geometry, $I_{RL}(\omega, T) = [1+n(\omega, T)][\chi''_{B_{1g}}(\omega, T) + \chi''_{B_{2g}}(\omega, T)] + L(\omega, T)$, is predominantly contributed by luminescent background. Therefore, we subtract signal in RL scattering geometry as a background from all measured spectra presented in this paper.

The coupling parameters in the Ginzburg-Landau free energy (Eq. 1) are chosen follow-

ing the recipes given in Haule and Kotliar^{28,39} with slight adjustments to match the phase diagram in Fig. 1a, with all energies and temperatures given in the units of kelvins, and all pressure units are in GPa. The quadratic couplings are defined as $\alpha_{HO}(\omega_0, T, P) \equiv -\frac{1}{2}J_{HO}(\omega_0, P) + \tilde{\alpha}_{HO}(\omega_0, T, P)$ and $\alpha_{AF}(\omega_0, T, P) \equiv -\frac{1}{2}J_{AF}(\omega_0, P) + \tilde{\alpha}_{AF}(\omega_0, T, P)$, where $\omega_0 = 35$ K is the effective energy separation between the singlet states in the minimal model, T is temperature, and P can be either hydrostatic pressure or effective chemical pressure. $J_{HO}(\omega_0, P) = \frac{\omega_0(1 + a_1P)}{\tanh\left(\frac{\omega_0}{2T_{HO}}\right)}$ and $J_{AF}(\omega_0, P) = \frac{\omega_0(1 + a_2P)}{\tanh\left(\frac{\omega_0}{2T_N}\right)}$ are the effective nearest neighbor exchange constants, with $T_{HO} = 17.5$ K and $T_N = 15.5$ K. $\tilde{\alpha}_{HO}(\omega_0, T, P) = \frac{1}{2}\omega_0 \coth\left(\frac{\omega_0}{2T}\right) (1 - a_3P)$ and $\tilde{\alpha}_{AF}(\omega_0, T, P) = \frac{1}{2}\omega_0 \coth\left(\frac{\omega_0}{2T}\right) (1 + a_3P)$ are the effective on-site couplings. $\beta(\omega_0, P) = \frac{\omega_0 \left[\sinh\left(\frac{\omega_0}{T}\right) - \frac{\omega_0}{T} \right] \cosh^2\left(\frac{\omega_0}{2T}\right)}{8 \sinh^4\left(\frac{\omega_0}{2T}\right)}$ is the quartic coupling.

* skung@physics.rutgers.edu

† girsh@physics.rutgers.edu

- ¹ Kanchanavatee, N. *et al.* Twofold enhancement of the hidden-order/large-moment antiferromagnetic phase boundary in the URu_{2-x}Fe_xSi₂ system. *Phys. Rev. B* **84**, 245122 (2011). URL <http://link.aps.org/doi/10.1103/PhysRevB.84.245122>.
- ² McElfresh, M. W. *et al.* Effect of pressure on competing electronic correlations in the heavy-electron system URu₂Si₂. *Phys. Rev. B* **35**, 43–47 (1987). URL <http://link.aps.org/doi/10.1103/PhysRevB.35.43>.
- ³ Jaime, M., Kim, K. H., Jorge, G., McCall, S. & Mydosh, J. A. High magnetic field studies of the hidden order transition in URu₂Si₂. *Phys. Rev. Lett.* **89**, 287201 (2002). URL <http://link.aps.org/doi/10.1103/PhysRevLett.89.287201>.
- ⁴ Kung, H.-H. *et al.* Chirality density wave of the “hidden order” phase in URu₂Si₂. *Science* **347**, 1339–1342 (2015). URL <http://www.sciencemag.org/content/347/6228/1339.abstract>.
- ⁵ Butch, N. P. *et al.* Antiferromagnetic critical pressure in URu₂Si₂ under hydrostatic conditions. *Phys. Rev. B* **82**, 060408 (2010). URL <http://link.aps.org/doi/10.1103/PhysRevB.82.060408>.
- ⁶ Jo, Y. J. *et al.* Field-induced fermi surface reconstruction and adiabatic continuity between antiferromagnetism and the hidden-order state in URu₂Si₂. *Phys. Rev. Lett.* **98**, 166404 (2007).

- URL <http://link.aps.org/doi/10.1103/PhysRevLett.98.166404>.
- ⁷ Haule, K. & Kotliar, G. Arrested Kondo effect and hidden order in URu₂Si₂. *Nature Phys.* **5**, 796–799 (2009). URL <http://www.nature.com/doi/10.1038/nphys1392>.
 - ⁸ Chandra, P., Coleman, P. & Flint, R. Hysteric order in the heavy-fermion compound URu₂Si₂. *Nature (London)* **493**, 621–626 (2013). URL <http://www.nature.com/nature/journal/v493/n7434/full/nature11820.html>.
 - ⁹ Hall, J. S. *et al.* Electrodynamics of the antiferromagnetic phase in URu₂Si₂. *Phys. Rev. B* **92**, 195111 (2015). URL <http://link.aps.org/doi/10.1103/PhysRevB.92.195111>.
 - ¹⁰ Palstra, T. T. M. *et al.* Superconducting and Magnetic Transitions in the Heavy-Fermion System URu₂Si₂. *Phys. Rev. Lett.* **55**, 2727–2730 (1985). URL <http://link.aps.org/doi/10.1103/PhysRevLett.55.2727>.
 - ¹¹ Maple, M. B. *et al.* Partially gapped Fermi surface in the heavy-electron superconductor URu₂Si₂. *Phys. Rev. Lett.* **56**, 185–188 (1986). URL <http://link.aps.org/doi/10.1103/PhysRevLett.56.185>.
 - ¹² Schlabitz, W. *et al.* Superconductivity and Magnetic Order in a Strongly Interacting Fermi-System: URu₂Si₂. *Z. Phys. B* **62**, 171–177 (1986). URL <http://dx.doi.org/10.1007/BF01323427>.
 - ¹³ Bourdarot, F. *et al.* Magnetic properties of URu₂Si₂ under uniaxial stress by neutron scattering. *Phys. Rev. B* **84**, 184430 (2011). URL <http://link.aps.org/doi/10.1103/PhysRevB.84.184430>.
 - ¹⁴ Schemm, E. R. *et al.* Evidence for broken time-reversal symmetry in the superconducting phase of URu₂Si₂. *Phys. Rev. B* **91**, 140506 (2015). URL <http://link.aps.org/doi/10.1103/PhysRevB.91.140506>.
 - ¹⁵ Aynajian, P. *et al.* Visualizing the formation of the Kondo lattice and the hidden order in URu₂Si₂. *Proc. Nat. Acad. Sci. USA* **107**, 10383–8 (2010). URL <http://www.pnas.org/content/107/23/10383.short>.
 - ¹⁶ Schmidt, A. R. *et al.* Imaging the Fano lattice to ‘hidden order’ transition in URu₂Si₂. *Nature (London)* **465**, 570–6 (2010). URL <http://www.nature.com/nature/journal/v465/n7298/full/nature09073.html>.
 - ¹⁷ Okazaki, R. *et al.* Rotational symmetry breaking in the hidden-order phase of URu₂Si₂. *Science* **331**, 439–42 (2011). URL <http://science.sciencemag.org/content/331/6016/439>.

- ¹⁸ Riggs, S. C. *et al.* Evidence for a nematic component to the hidden-order parameter in URu₂Si₂ from differential elastoresistance measurements. *Nat Commun* **6** (2015). URL <http://dx.doi.org/10.1038/ncomms7425>.
- ¹⁹ Mydosh, J. A. & Oppeneer, P. M. Colloquium: Hidden order, superconductivity, and magnetism: The unsolved case of URu₂Si₂. *Rev. Mod. Phys.* **83**, 1301–1322 (2011). URL <http://link.aps.org/doi/10.1103/RevModPhys.83.1301>. And references therein.
- ²⁰ Hassinger, E. *et al.* Temperature-pressure phase diagram of URu₂Si₂ from resistivity measurements and ac calorimetry: Hidden order and fermi-surface nesting. *Phys. Rev. B* **77**, 115117 (2008). URL <http://link.aps.org/doi/10.1103/PhysRevB.77.115117>.
- ²¹ Broholm, C. *et al.* Magnetic excitations and ordering in the heavy-electron superconductor URu₂Si₂. *Phys. Rev. Lett.* **58**, 1467–1470 (1987). URL <http://link.aps.org/doi/10.1103/PhysRevLett.58.1467>.
- ²² Williams, T. *et al.* Gapped excitations in the high-pressure antiferromagnetic phase of URu₂Si₂. *arXiv:1607.00967* (2016). URL <http://arxiv.org/abs/1607.00967>.
- ²³ Ran, S. *et al.* Phase diagram and thermal expansion measurements on the system of URu_{2-x}Fe_xSi₂. *arXiv:1604.00983* (2016). URL <http://arxiv.org/abs/1604.00983>.
- ²⁴ Wilson, M. N. *et al.* Antiferromagnetism and hidden order in isoelectronic doping of URu₂Si₂. *Phys. Rev. B* **93**, 064402 (2016). URL <http://link.aps.org/doi/10.1103/PhysRevB.93.064402>.
- ²⁵ Das, P. *et al.* Chemical pressure tuning of URu₂Si₂ via isoelectronic substitution of Ru with Fe. *Phys. Rev. B* **91**, 085122 (2015). URL <http://link.aps.org/doi/10.1103/PhysRevB.91.085122>.
- ²⁶ Butch, N. P. *et al.* Distinct magnetic spectra in the hidden order and antiferromagnetic phases in URu_{2-x}Fe_xSi₂. *arXiv:1607.02136* (2016). URL <http://arxiv.org/abs/1607.02136>.
- ²⁷ Williams, T. J., Wilson, M. N., Aczel, A. A., Stone, M. B. & Luke, G. M. Hidden Order Signatures in the Antiferromagnetic Phase of U(Ru_{1-x}Fe_x)₂Si₂. *arXiv:1607.05672* (2016). URL <http://arxiv.org/abs/1607.05672>.
- ²⁸ Haule, K. & Kotliar, G. Complex Landau-Ginzburg theory of the hidden order in URu₂Si₂. *Europhys. Lett.* **89**, 57006 (2010). URL <http://stacks.iop.org/0295-5075/89/i=5/a=57006>.
- ²⁹ Khveshchenko, D. V. & Wiegmann, P. B. Raman scattering and anomalous current algebra in mott insulators. *Phys. Rev. Lett.* **73**, 500–503 (1994). URL <http://link.aps.org/doi/10.1103/PhysRevLett.73.500>.

- [1103/PhysRevLett.73.500](http://link.aps.org/doi/10.1103/PhysRevLett.73.500).
- ³⁰ Guo, W. T. *et al.* Hybridization gap versus hidden-order gap in URu₂Si₂ as revealed by optical spectroscopy. *Phys. Rev. B* **85**, 195105 (2012). URL <http://link.aps.org/doi/10.1103/PhysRevB.85.195105>.
- ³¹ Lobo, R. P. S. M. *et al.* Optical conductivity of URu₂Si₂ in the kondo liquid and hidden-order phases. *Phys. Rev. B* **92**, 045129 (2015). URL <http://link.aps.org/doi/10.1103/PhysRevB.92.045129>.
- ³² Hall, J. S. *et al.* Observation of multiple-gap structure in hidden order state of URu₂Si₂ from optical conductivity. *Phys. Rev. B* **86**, 035132 (2012). URL <http://link.aps.org/doi/10.1103/PhysRevB.86.035132>.
- ³³ Pfeleiderer, C., Mydosh, J. A. & Vojta, M. Pressure dependence of the magnetization of URu₂Si₂. *Phys. Rev. B* **74**, 104412 (2006). URL <http://link.aps.org/doi/10.1103/PhysRevB.74.104412>.
- ³⁴ Cooper, S. L., Klein, M. V., Maple, M. B. & Torikachvili, M. S. Magnetic excitations and phonon anomalies in URu₂Si₂. *Phys. Rev. B* **36**, 5743–5746 (1987). URL <http://link.aps.org/doi/10.1103/PhysRevB.36.5743>.
- ³⁵ Buhot, J. *et al.* Symmetry of the excitations in the hidden order state of URu₂Si₂. *Phys. Rev. Lett.* **113**, 266405 (2014). URL <http://link.aps.org/doi/10.1103/PhysRevLett.113.266405>.
- ³⁶ Levallois, J. *et al.* Hybridization gap and anisotropic far-infrared optical conductivity of URu₂Si₂. *Phys. Rev. B* **84**, 184420 (2011). URL <http://link.aps.org/doi/10.1103/PhysRevB.84.184420>.
- ³⁷ Niklowitz, P. G. *et al.* Role of commensurate and incommensurate low-energy excitations in the paramagnetic to hidden-order transition of URu₂Si₂. *Phys. Rev. B* **92**, 115116 (2015). URL <http://link.aps.org/doi/10.1103/PhysRevB.92.115116>.
- ³⁸ Niklowitz, P. G. *et al.* Parasitic Small-Moment Antiferromagnetism and Nonlinear Coupling of Hidden Order and Antiferromagnetism in URu₂Si₂ Observed by Larmor Diffraction. *Phys. Rev. Lett.* **104**, 106406 (2010). URL <http://link.aps.org/doi/10.1103/PhysRevLett.104.106406>.
- ³⁹ Boyer, L. & Yakovenko, V. A model for the polar kerr effect in the hidden-order phase of URu_{2-x}Fe_xSi₂. *APS March Meeting Baltimore Abstracts* **R22**, 4 (2016). URL [http:](http://)

[//meetings.aps.org/link/BAPS.2016.MAR.R22.4](http://meetings.aps.org/link/BAPS.2016.MAR.R22.4).

- ⁴⁰ Matsuda, K., Kohori, Y., Kohara, T., Kuwahara, K. & Amitsuka, H. Spatially inhomogeneous development of antiferromagnetism in URu₂Si₂: Evidence from ²⁹Si NMR under pressure. *Phys. Rev. Lett.* **87**, 087203 (2001). URL <http://link.aps.org/doi/10.1103/PhysRevLett.87.087203>.
- ⁴¹ Yokoyama, M. *et al.* Competition between hidden order and antiferromagnetism in URu₂Si₂ under uniaxial stress studied by neutron scattering. *Phys. Rev. B* **72**, 214419 (2005). URL <http://link.aps.org/doi/10.1103/PhysRevB.72.214419>.
- ⁴² Bardasis, A. & Schrieffer, J. R. Excitons and plasmons in superconductors. *Phys. Rev.* **121**, 1050–1062 (1961). URL <http://link.aps.org/doi/10.1103/PhysRev.121.1050>.
- ⁴³ Ovander, L. N. The form of the Raman tensor. *Optics and Spectroscopy* **9**, 302 (1960).